PAPER

Nanoshaping of glass forming metallic liquids by stretching: evading lithography

IOP Publishing Nanotechnology
Nanotechnology 30 (2019) 075302 (11pp) https://doi.org/10.1088/1361-6528/aaf3db

Nanoshaping of glass forming metallic liquids by stretching: evading lithography

Zhonglue Hu, Chandra Sekhar Meduri, Jerzy Blawzdziewicz and Golden Kumar[1]

Department of Mechanical Engineering, Texas Tech University, Lubbock, TX 79409, United States of America

E-mail: Golden.Kumar@UTDallas.edu

Received 30 September 2018, revised 20 November 2018
Accepted for publication 26 November 2018
Published 18 December 2018

Abstract

Lithography-free nanomanufacturing by elongation and fracture of glass forming metallic liquid is presented. The viscous metallic liquid confined in a cavity is laterally downsized to nanoscale by stretching. The extent of size-reduction can be controlled by tuning the active volume of liquid and the viscous and capillary stresses. Very high aspect-ratio metal nanostructures can be fabricated without using lithography or expensive molds. A systematic study is performed using glass forming Pt-Cu-Ni-P alloy to understand the effects of viscosity, surface tension, pulling velocity, and cavity size on the evolution of cylindrical liquid column under tension. The results are quantitatively described using a phenomenological model based on lubrication theory and surface tension induced breakup of liquid filaments. A new manufacturing approach based on variable pulling velocity and/or spinning of metallic liquid is proposed for fabrication of complex geometries.

Supplementary material for this article is available online

Keywords: nanofabrication, metallic glass, fiber drawing

(Some figures may appear in colour only in the online journal)

1. Introduction

Metallic glasses (MGs) are known for their large elastic strain limit, high hardness, and good wear and corrosion resistance [1–5]. These properties are homogeneous and isotropic down to nanometer scale owing to the featureless amorphous structure of MGs [6–8]. The attractive combination of mechanical properties and homogeneous structure makes MGs good candidates for metal components in nanoscale devices [9–14]. Thus, cost-effective fabrication of MG nanostructures becomes crucial to exploit their potential in nanoscale applications. MGs exhibit metastable supercooled liquid state which has enabled thermoplastic processing of MGs like polymers or oxide glasses. Among various techniques, thermoplastic embossing has emerged as a promising nanofabrication approach for MGs due to its ease in implementation [15–19].

Though thermoplastic embossing of MGs shows great potential for nanofabrication, high pressure at nanoscale and need for expensive templates remain as major manufacturing challenges. Silicon (Si) templates prepared by lithography are a preferred choice due to excellent dimensional accuracy [20–23], but the associated high cost and the fragile nature of Si templates limit their usability. Besides, embossing is not practical for high aspect-ratio nanostructures because of the rapid increase in pressure with feature length [15, 16, 24]. One-dimensional nanostructures such as nanowires and nanotubes are desirable for many applications such as, catalysts [25, 26], sensors [27–30], electrodes [11, 12, 31, 32], and light trapping architectures [33, 34], because of large surface to volume ratio. Longer length also facilitates mechanical [35–37], thermal [38], and electrical [39, 40] testing of individual nanostructures to characterize the size-effects. Recent studies suggest that the pressure limitation for

[1] Present address: The University of Texas at Dallas, Richardson, TX 75080, USA.

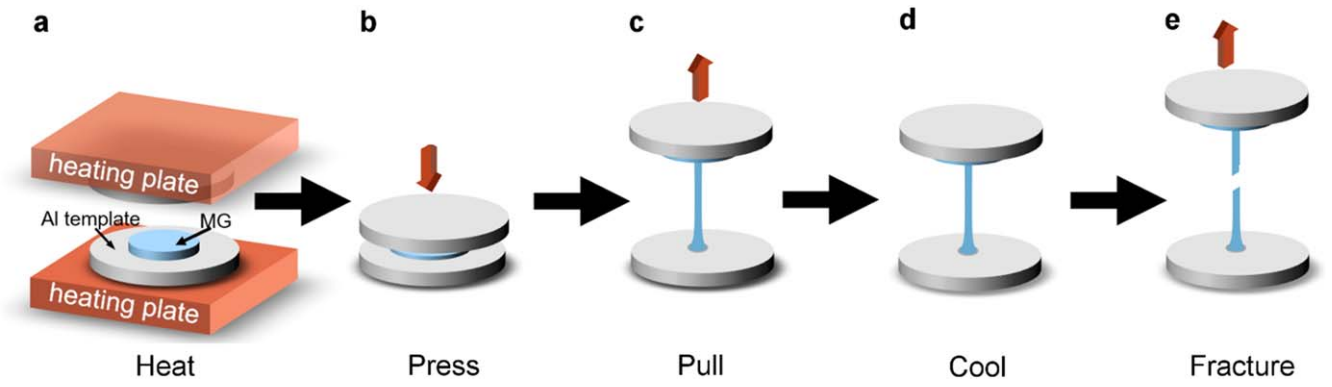

Figure 1. Schematic illustration of thermoplastic drawing procedure. (a) A disk of MG is placed on top of a cylindrical cavity machined in Al. The entire set-up is heated above T_g using two heating plates. The plates are not shown in subsequent steps to avoid redundancy. (b) The movable top plate embosses the MG into the Al cavity. The top plate is designed to anchor with the MG disk. (c) The top plate is moved upward while subjecting the MG in cavity to tensile deformation. The velocity and displacement of top plate are controllable variables. (d) The set-up is cooled to room temperature after achieving a preset extensional displacement. (e) The MG is fractured into two symmetric parts for subsequent SEM characterization.

embossing of high aspect-ratio nanostructures can be overcome by using thermoplastic drawing (pulling) in MGs [35, 41]. However, lithographically made templates were still required to attain nanoscale features [42]. Moreover, the quantitative correlation between the drawing parameters and the size or shape of generated nanostructures has not been established. For example, processing conditions (MG viscosity, strain-rate, and starting dimensions) required for a desirable nanostructure cannot be inferred from the previous studies on drawing [35, 41, 42]. Such knowledge, however, is critical to develop a deterministic and reproducible nanomanufacturing based on thermoplastic drawing of MGs.

The objective of present work is two-fold. First, we demonstrate that MG structures as large as 100–500 μm (attainable through machining) can be controllably downsized to sub-100 nm (2000 times reduction) by drawing. Such dramatic size-reduction by mechanical deformation is an important breakthrough in metal nanomanufacturing because it demonstrates the fabrication of nanostructures without expensive lithography or molds. Second, we develop a quantitative correlation between the governing parameters and the outcome of MG drawing in the supercooled liquid state. The effects of key processing parameters: starting dimensions, temperature, and drawing velocity on the final shape and size of structure are studied using an example of Pt-based MG. The experimental results are used to verify the proposed model for drawing. We further show that unparalleled geometries can be manufactured by integrating variable velocity or rotational motion during thermoplastic drawing of MGs.

2. Thermoplastic drawing

$Pt_{57.5}Cu_{14.7}Ni_{5.3}P_{22.5}$ (At%) metallic glass (Pt-MG) was used as a model material because of its good thermoplastic forming ability and oxidation resistance. Pt-MG was synthesized by water quenching as described in literature [16]. The glass transition temperature (T_g) and the crystallization temperature (T_x) of Pt-MG are 230 °C and 309 °C, respectively. The present study focuses on thermoplastic elongation of a single MG structure in order to quantify the reshaping process. Figure 1 shows the schematic illustration of drawing set-up used in this work. Single cylindrical cavities (diameter = 100–500 μm and length = 3 × diameter) were mechanically drilled in aluminum (Al) substrates. The Al template was fixed to the bottom heating plate and a disk of Pt-MG was positioned on top of the cylindrical cavity (figure 1(a)). The surrounding area of cavity was covered with a thin polyvinylidene difluoride tape to prevent sticking of MG disk with Al. After heating the entire set-up above T_g, the top plate was moved downwards to emboss the Pt-MG into the cavity (figure 1(b)). The movable top plate in our set-up was designed to strongly anchor to the MG disk during embossing. Subsequently, the top plate and the anchored MG disk were pulled upward at a constant velocity while subjecting the MG supercooled liquid in Al cavity to tensile deformation (figure 1(c)). The pulling velocity and the displacement (or time) were controlled but the tensile force was not recorded, as the force was below the detection limit of our load cell. After reaching a desired extensional displacement, the set-up was cooled down to room temperature (figure 1(d)) and the fiber was fractured in two symmetric parts for scanning electron microscopy (SEM) characterization (figure 1(e)). Under certain conditions, the fiber necked and ruptured during thermoplastic elongation. Amorphous state of representative specimens after drawing was verified using differential scanning calorimetry.

3. Results and discussion

The results and discussion are organized in four sub-sections. In section 3.1, we present the effects of key drawing variables on the shape of MG fiber and analyze the results in terms of hydrodynamic dimensionless numbers. Section 3.2 focuses on the evolution of fiber diameter during elongation. An analytical description of the diameter reduction is developed to predict the minimum diameter achievable by elongation

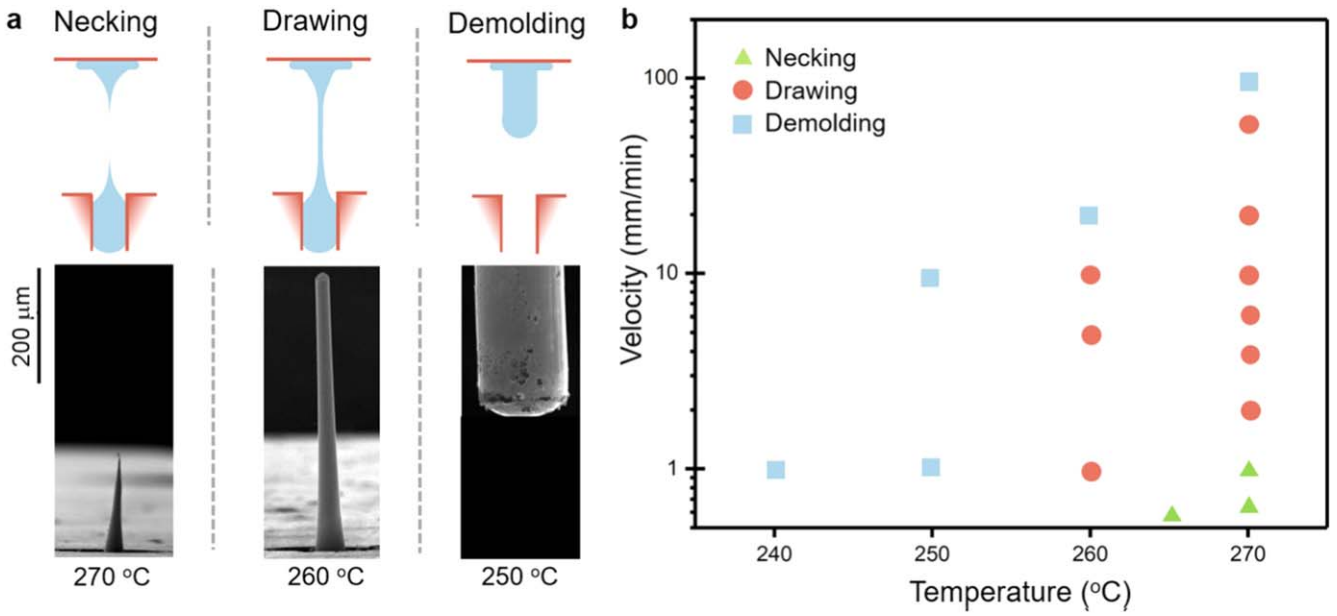

Figure 2. Effects of drawing temperature and velocity on the morphology of MG drawn from a cylindrical cavity. (a) Schematics and SEM images show three typical morphologies (necking, drawing, and demolding) observed while drawing at a constant velocity (1 mm min^{-1}) but different temperatures. (b) Results from varying temperatures and velocities are combined to construct a morphology map for thermoplastic drawing of Pt-MG. All the data are for a constant elongation of 3 mm and cavity diameter of 200 μm.

before breakup. Section 3.3 describes how the active volume of MG supercooled liquid participating in elongation can be controlled through drawing conditions. Active liquid volume plays an important role in determining the extent of diameter reduction under practical elongations. In the last section, we demonstrate the versatility of drawing-based manufacturing by incorporating variable velocity or rotational motion during elongation.

3.1. Drawing morphologies

The SEM analysis reveals that there are two key parameters which control the morphology of MG drawn in the supercooled liquid state: temperature and drawing velocity (figure 2). Temperature affects the viscosity and the surface tension of MG supercooled liquid whilst the drawing velocity determines the strain-rate. As shown in figure 2(a), three distinct morphologies evolve as a function of temperature (250 °C–270 °C) when the Pt-MG liquid is drawn from a cylindrical cavity at a constant velocity (1 mm min^{-1}). This temperature range is selected to avoid the crystallization which makes the drawing process highly irreproducible. High temperature (270 °C) drawing results in profuse necking and breakup into two sharp conical structures. In contrast, a long fiber with relatively uniform diameter is drawn at an intermediate temperature (260 °C). The fiber did not break during drawing but was subsequently fractured at room temperature for imaging. Further decrease in processing temperature (250 °C) causes complete separation of MG from the cavity. We categorize the three morphologies as: necking, drawing, and demolding. It is important to note that the distinction between necking and drawing shown in figure 2 is applicable only for a fixed elongation (in this case 3 mm) because the drawing sample undergoes a necking instability at longer elongations. Similar morphologies were also observed when the drawing velocity was varied at a constant temperature. The data from the temperature and the velocity experiments are combined to construct a morphology map as shown in figure 2(b). The results indicate that decrease in processing temperature or increase in drawing velocity has the same effect on the shape of MG. Both these changes result in a transition from necking to drawing and eventually to demolding.

The demolding is observed when the stress required to deform MG supercooled liquid (flow stress) is higher than its adhesive strength with the mold, as explained in our previous work [43]. The necking and drawing morphologies are observed when the MG supercooled liquid strongly adheres to the mold during pulling. The formation of necking or drawing morphologies can be understood by comparing the relative effects of viscous and capillary stresses on the elongating MG fiber. These effects can be quantified using dimensionless capillary number (Ca) [44–46]:

$$Ca = \frac{viscous\ stress}{capillary\ stress} = \frac{\eta v/L}{\gamma/D}, \tag{1}$$

where η is the MG viscosity, v is the drawing velocity, L is the instantaneous length of MG fiber, γ is the MG surface tension, and D is the smallest diameter of fiber. The necking induced by the surface tension is opposed by the viscous resistance. Therefore, higher Ca favors uniform elongation whereas lower Ca results in necking. This is consistent with the observed effects of temperature and drawing velocity on the fiber morphology (figure 2(b)). The Ca decreases during

Table 1. Experimental conditions (temperature, viscosity, drawing velocity, and total elongation) and the resulting final diameter of Pt-MG pulled from 200 μm diameter cavity. The capillary number calculated from the final diameter and the fiber morphology are also listed. The value of surface tension, $\gamma = 1\ \mathrm{N\ m^{-1}}$ was used.

Temperature (°C)	Viscosity (10^7 Pa s)	Velocity (mm min^{-1})	Elongation (mm)	Minimum diameter (μm)	Final capillary number	Morphology
250	24.5	1	3	100	136	*Demolding*
260	5.5	1	3	13.9	4.24	*Drawing*
		6	3	14.4	26.4	*Drawing*
		6	22	0.201	0.05	*Necking*[a]
		20	3	100	611	*Demolding*
270	1.4	1	3	0.075	0.006	*Necking*[a]
		10	3	20	14.1	*Drawing*
		10	8	7.1	1.27	*Drawing*
		10	13	1.6	0.287	*Drawing*
		10	25	0.4	0.03	*Necking*[a]
		20	3	10.3	16.4	*Drawing*
		20	8	7.9	4.6	*Drawing*
		20	13	4.7	1.68	*Drawing*
		20	25	0.161	0.03	*Necking*[a]
		30	3	16.6	38.7	*Drawing*
		30	8	5.05	4.41	*Drawing*
		30	45	0.15	0.023	*Necking*[a]
		100	3	100	7941	*Demolding*

[a] The samples ruptured during elongation due to necking instability at low capillary numbers.

elongation due to increasing L and decreasing D (table 1). Below a critical Ca (~0.1), rapidly growing necking instability results in fiber breakup. Therefore, the final breakup is always dictated by the capillary induced necking. We have ruled out the other possible causes for drawing-to-necking transition such as, temperature gradient and non-Newtonian effects. Temperature was measured at different locations between the heating plates. The variation in temperature was less than ±2 °C in the range of 50 °C–300 °C. Such small change in temperature (or associated viscosity) during elongation is not sufficient to account for the observed sample morphologies. As for the non-Newtonian effect, the strain-rates estimated from the drawing velocities are much smaller than the ones reported for Newtonian to non-Newtonian transition in Pt-MG at comparable temperatures [47–49]. Therefore, the Pt-MG supercooled liquid can be considered as a Newtonian fluid in current drawing experiments.

3.2. Diameter evolution

A closer look at the MG fibers reveals that thermoplastic drawing can generate nanoscale geometries without lithography or nanomolds (supporting information figure S1 is available online at stacks.iop.org/NANO/30/075302/mmedia). For example, slow drawing from a 200 μm diameter cavity results in nearly 2000-fold reduction in diameter before rupture, forming nanotips with sub-100 nm diameters. However, such dramatic reduction in size is accessible only either at high temperatures or slow drawing velocities (necking regime in figure 2), both of which impose the risk of crystallization and embrittlement in MGs [50]. It would be beneficial if MG nanostructures can be formed in the drawing regime which is observed at low temperatures and/or higher drawing velocities. To test this possibility, we analyze the evolution of MG fiber diameter through systematic drawing experiments and analytical description.

The fiber diameter during drawing is expected to depend on the extensional strain and the initial diameter. A series of drawing experiments were carried out to quantify the effects of elongation (L_e) and the cavity diameter (D_o) on the minimum fiber diameter ($D_{\min}$) for Pt-MG (figure 3). The processing temperature (270 °C) and the velocity (10 mm min^{-1}) were selected in the drawing regime shown in figure 2. Figures 3(a) and (b) show the effects of varying L_e and D_o, respectively. The SEM images of representative specimens demonstrate the formation of uniform and smooth MG fibers with nanoscale diameters. The fibers showed no detectable voids during cross-sectional analysis. The minimum diameter $D_{\min}$ decreases with increasing L_e or decreasing D_o. However, these results could not be explained by the deformation of entire liquid volume contained in cavities. The control over the active volume of MG in thermoplastic drawing is desirable for predictable diameter reduction and it will be analyzed in section 3.3.

The evolution of fiber diameter can be quantitatively analyzed using a lubrication theory for a filament of high-viscosity Newtonian fluid undergoing uniaxial extension. The assumptions of Newtonian behavior and creeping-flow are valid for the MG supercooled liquid in current drawing experiments. As explained in section 3.1, not only the viscous but also the capillary stresses are important in determining the filament morphology. However, the lubrication theory that includes capillary stress can be solved only numerically. Therefore, we propose an approximate expression that describes the evolution of $D_{\min}$ over the entire drawing range and incorporates both viscous and capillary effects. The

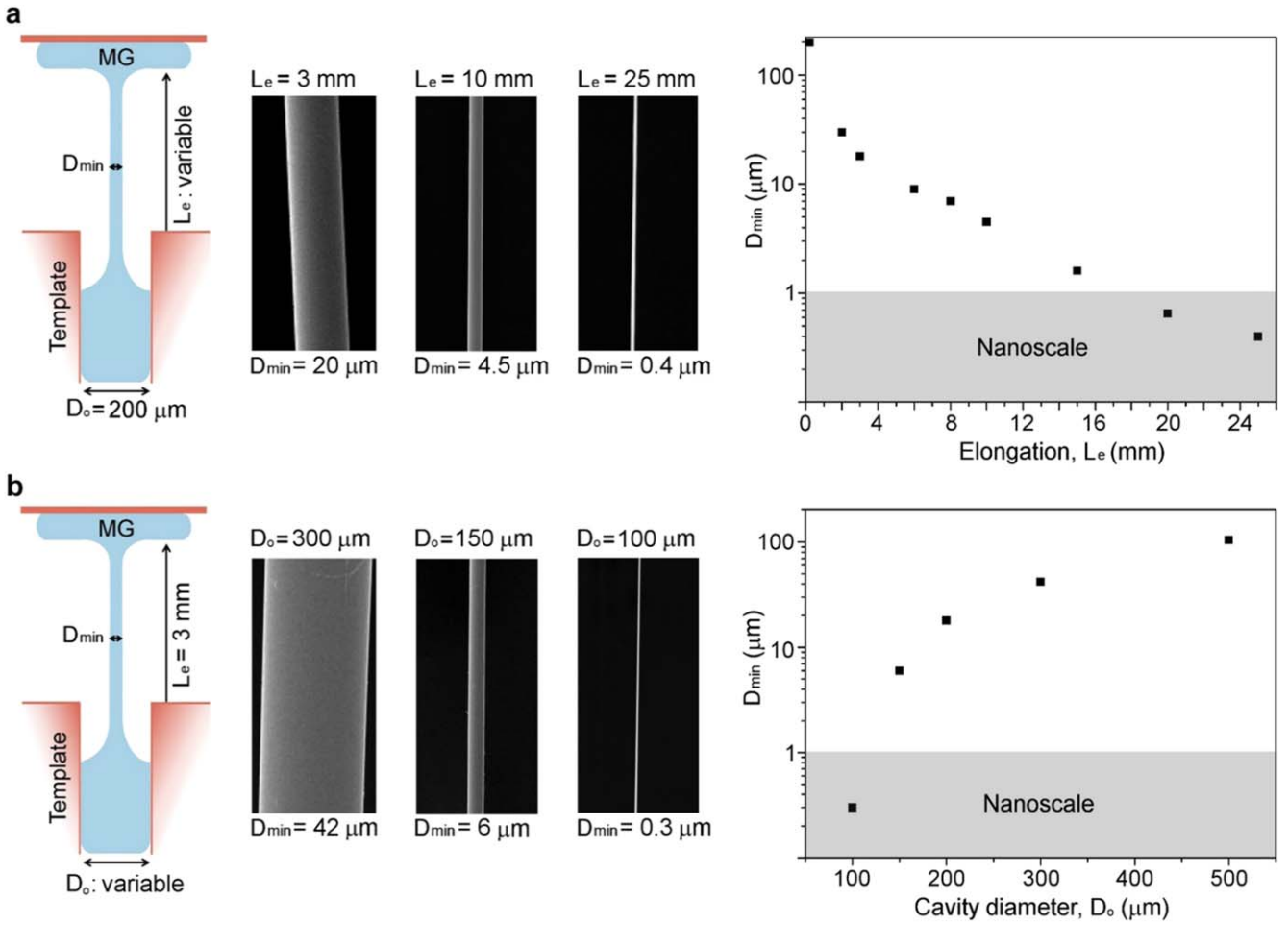

Figure 3. Dependence of minimum fiber diameter ($D_{\min}$) on elongation (L_e) and cavity diameter (D_o) during thermoplastic drawing. (a) $D_{\min}$ as a function of L_e and (b) $D_{\min}$ as a function of D_o for Pt-MG drawn at 270 °C and velocity of 10 mm min^{-1}. SEM images of selected samples for variable L_e and D_o are also shown.

approximation is obtained by combining the results of a purely viscous lubrication analysis to characterize the initial fiber evolution with the similarity solution to account for the capillary induced necking.

As discussed in supporting information (section 2), the evolution of $D_{\min}$ in the absence of surface tension can be obtained using a lubrication description in Lagrangian coordinates [51] and a small perturbation assumption for the initial filament shape. The resulting expression for $D_{\min}$, normalized by D_o becomes:

$$\frac{D_{\min}}{D_o} \propto \frac{\pi}{\frac{\alpha L_e}{D_o} + 2}, \tag{2}$$

where α is a fitting parameter associated with the initial condition. Figure 4(a) compares the experimental and the calculated values of $D_{\min}/D_o$ for varying L_e normalized by D_o. The theoretical and the measured values match well for relatively short fibers, but significant deviation occurs at longer lengths. The deviation is caused by the rising capillary stress as the fiber diameter shrinks during drawing.

The effect of capillary stress can be accounted for by using the similarity analysis of the evolution of liquid filament shape near the breakup time. According to the Papageorgiou's similarity solution [52], the minimum diameter linearly decays to zero and the breakup occurs at finite time t_B:

$$\frac{D_{\min}}{D_o} \propto \left(1 - \frac{t}{t_B}\right), \tag{3}$$

where t_B depends on the surface tension, the viscosity, and the initial diameter of fiber (section 3 in supporting information). The value of t_B can be calculated as described in the literature [52, 53] or can be measured experimentally from the length of fiber at breakup L_B ($=v \times t_B$). It is worth noting that the lubrication theory without surface tension (equation (2)) predicts continuous thinning of fiber without imminent rupture. In contrast, the surface tension driven flow (equation (3)), predicts a finite time singularity in the fiber diameter. We propose a phenomenological factorization relation that combines equations (2) and (3) to describe the fiber diameter over a wide range of elongations:

$$\frac{D_{\min}}{D_o} \propto \left(\frac{\pi}{\frac{\alpha L_e}{D_o} + 2}\right)\left(1 - \frac{t}{t_B}\right) = \left(\frac{\pi}{\frac{\alpha L_e}{D_o} + 2}\right)\left(1 - \frac{L_e}{L_B}\right). \tag{4}$$

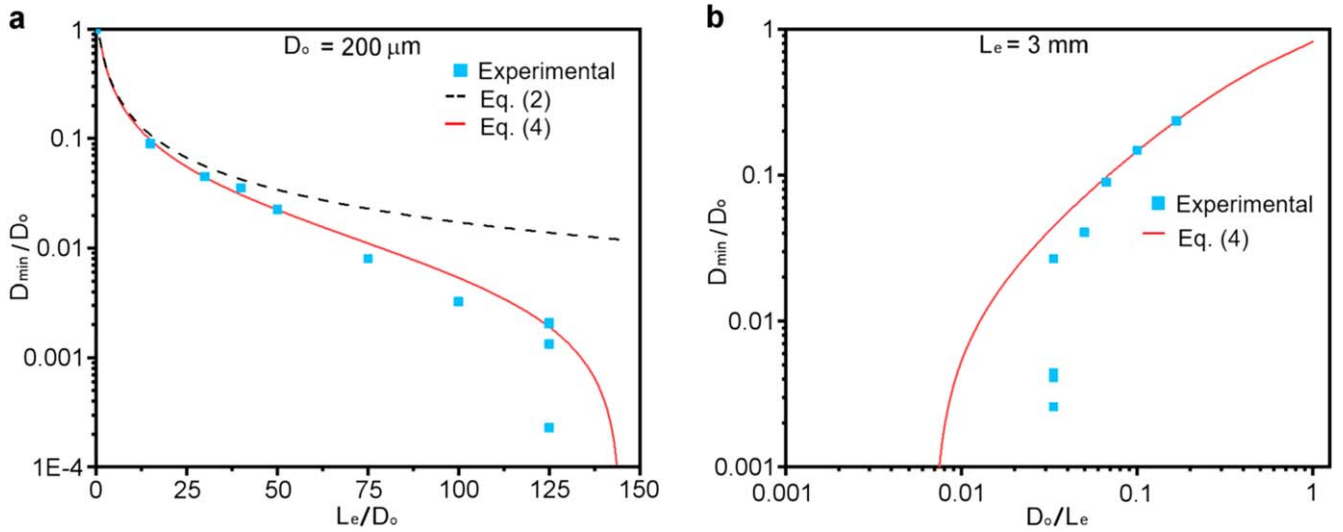

Figure 4. A comparison between the measured and the theoretical values of dimensionless minimum fiber diameter $D_{\min}/D_o$. The results are plotted (a) versus L_e/D_o for constant $D_o = 200$ μm, and (b) versus D_o/L_e for constant $L_e = 3$ mm. The symbols represent the experimental values, and the solid line is the prediction of the phenomenological model equation (4). In panel (a), the approximate lubrication analysis result, equation (2), is also shown (dashed line) to highlight the effect of surface tension.

As shown in figure 4(a), equation (4) accurately captures the decrease in the fiber diameter even at longer elongations. The deviation from the measured values in the singularity regime (i.e., where t approaches t_B) is caused by the scatter in experimental data. The breakup process during the capillary induced necking instability is highly sensitive to surface perturbations or any fluctuation in experimental conditions. Multiple drawing experiments conducted to same L_e values in the singularity regime clearly demonstrate the stochastic nature of fiber breakup (figure 4(a)).

A similar observation can be made for MG fibers subjected to the same elongation L_e but from cavities of different diameters (figure 4(b)). Equation (4) accurately describes the diameter evolution for large D_o but a notable discrepancy arises when the D_o/L_e ratio approaches singularity regime, where the experimental data are highly scattered. The findings from two different sets of experiments with varying L_e (figure 4(a)) or D_o (figure 4(b)) indicate that equation (4) can be used to describe the MG fiber diameter during drawing until the onset of singularity. In the necking regime, equation (4) yields an upper limit for $D_{\min}/D_o$. The quantitative correlation allows us to predict the fiber diameter, thus making the drawing-based manufacturing more controllable and reproducible. The diameter of thermoplastically drawn MG fibers can be tailored by varying the elongation, cavity size, viscosity, and pulling velocity according to equation (4). It should be noted that equation (4) is an approximate solution but more accurate quantitative description can be achieved using the numerical solution of lubrication theory detailed in supporting information.

3.3. Active volume of MG supercooled liquid

The active volume fraction of MG supercooled liquid plays an important role in determining the extent of diameter reduction predicted by equation (4), by affecting the fitting parameter (α) related to initial conditions. Smaller active volume facilitates rapid decrease in diameter at a shorter elongation, which is desirable for practical nanomanufacturing. In this section, we analyze the effects of various drawing parameters on the active (deformed) volume fraction of MG supercooled liquid.

Figure 5 shows the effect of extensional displacement on the active volume of MG supercooled liquid. The schematic illustrations (not to scale) are based on the SEM images to facilitate the understanding of drawing process. To determine the time evolution of the active liquid volume, a series of drawing experiments were stopped at different elongations (0.1–30 mm) while keeping all other parameters constant. After each drawing test, the residual MG was released from the template for SEM analysis to measure the deformed length (L_d), which is proportional to the active volume. As the SEM images indicate, at earlier stages of drawing, the triple contact-line moves downwards and the volume fraction of MG participating in the drawing increases rapidly. As the elongation further increases, the deformation becomes localized at the thinner section of MG and the contact-line gets pinned. Beyond this transition in contact-line dynamics, the volume of MG subjected to elongation remains largely unaffected as demonstrated by the SEM images after elongations of 3 and 30 mm.

Drawing experiments were also conducted for varying cavity diameters and velocities to quantify their influence on the active volume fraction of MG supercooled liquid. The values of L_d as a function of L_e, D_o, and v calculated from the corresponding SEM images are plotted in figure 6. For example, change in L_d versus L_e is measured from multiple SEM images like the ones shown in figure 5. The large scatter in data is caused by inherent variation in machined cavities used in different experiments. Despite scatter, the trend is clear and L_d appears to level off after initial rise with increasing L_e (figure 6(a)). In contrast, L_d monotonically increases with drawing velocity (figure 6(b)). At very high

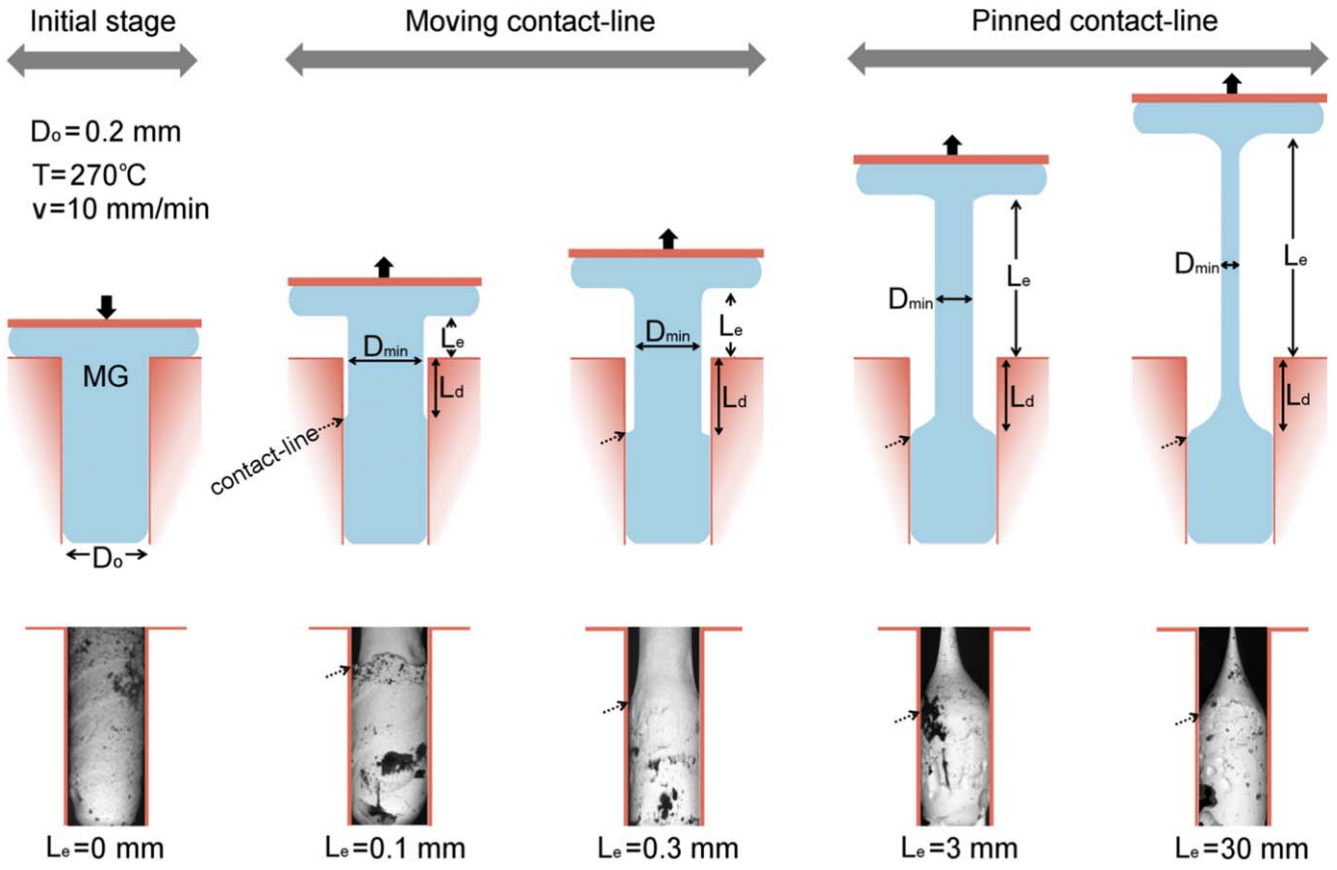

Figure 5. Evolution in deformed length (L_d) of MG cylinder participating in drawing. The sketches (not to scale) are based on the SEM images of Pt-MG drawn to varying L_e. The drawing velocity, temperature, and cavity diameter were 10 mm min^{-1}, 270 °C, and 200 μm, respectively. Initially L_d increases with L_e (moving contact-line) but remains unchanged at longer L_e (pinned contact-line).

drawing velocity (e.g. 100 mm min^{-1} or higher), the entire MG cylinder demolds from the template. Increasing trend in L_d is also observed for increasing cavity diameter (figure 6(c)). Here, we propose a simplified model to rationalize the dependence of L_d on drawing parameters.

The drawing of MG supercooled liquid from a template can be considered as a competition between the adhesion at the MG-template interface and the deformation of MG. At the initial stage when the tensile force is ramped up from zero, the force is not sufficient to overcome the flow stress of MG supercooled liquid because of large cross-sectional area. The increasing force, however, surpasses the critical pull-off force (F_c) and gradually dewets the MG supercooled liquid from the template (increasing L_d). The energy required to dewet the MG supercooled liquid per unit area is given by the work of adhesion:

$$W_{adh} = \gamma(1 + \cos\theta), \tag{5}$$

where θ is the contact angle between the MG supercooled liquid and the template, and γ is the surface tension of MG supercooled liquid. Such dewetting process of MG supercooled liquid from the cavity wall is analogous to peeling off an adhesive tape where the critical pull-off force can be written in terms of work of adhesion [54, 55]:

$$F_c = W_{adh}\pi D_o, \tag{6}$$

The dewetting process continues until the force required to deform the MG fiber (F_d) becomes smaller than the pull-off force. The F_d can be written as:

$$F_d = \sigma_f \frac{\pi D_{\min}^2}{4}, \tag{7}$$

where σ_f is the flow stress of MG supercooled liquid. Assuming the MG supercooled liquid as a Newtonian fluid, the flow stress can be expressed as:

$$\sigma_f = 3\eta\dot{\epsilon} = 3\eta\frac{v}{L}, \tag{8}$$

where η is the viscosity of MG supercooled liquid, $\dot{\epsilon}$ is the strain-rate, and L ($=L_d + L_e$) is the instantaneous length of MG fiber (figure 5). Substitution of σ_f in equation (7) yields:

$$F_d = 3\eta\frac{v}{L_d + L_e}\frac{\pi D_{\min}^2}{4}, \tag{9}$$

The contact-line motion ceases when the decreasing F_d (equation (9)) reaches F_c (equation (6)) and further drawing only results in elongation and thinning of MG fiber. Therefore, L_d can be obtained by combining equations (6) and (9).

$$L_d = \frac{3\eta v D_{\min}^2}{4W_{adh}D_o} - L_e, \tag{10}$$

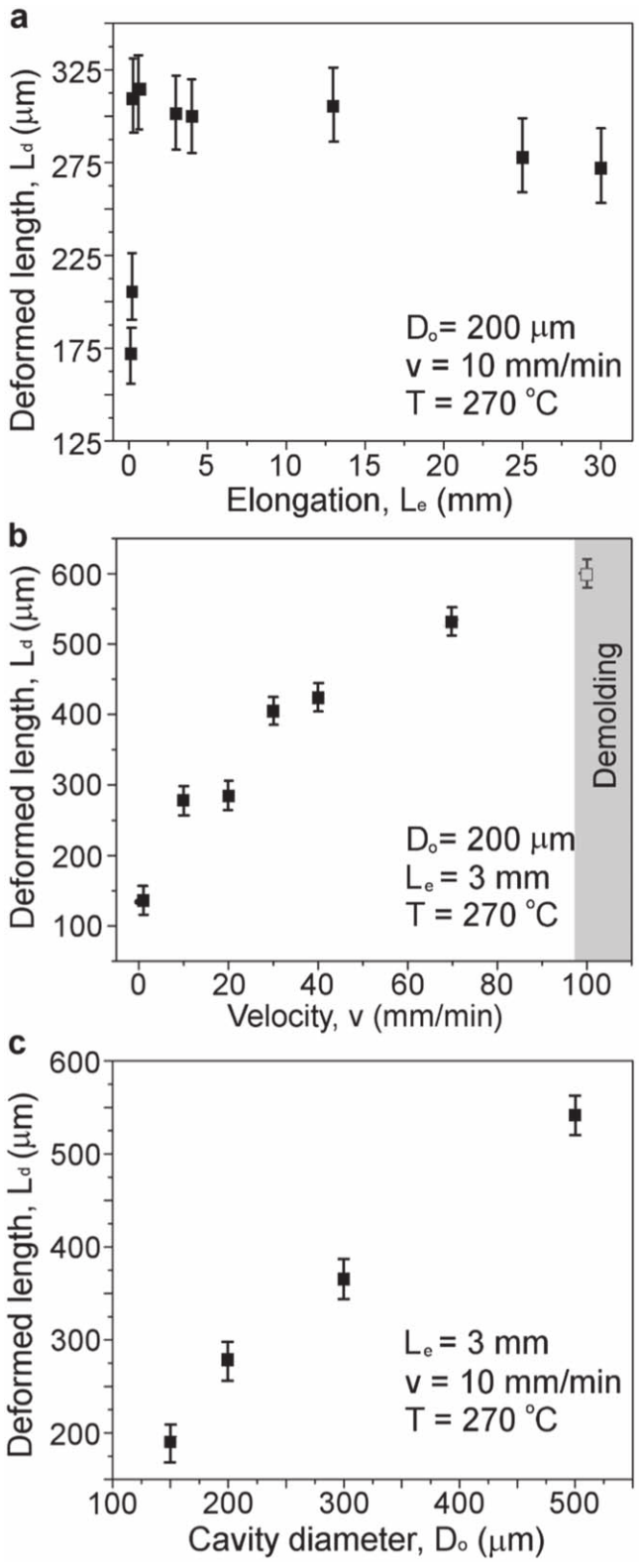

Figure 6. Dependence of deformed length (L_d) on various drawing parameters for Pt-MG. (a) L_d remains independent of elongation L_e., except during the initial transient stage. Large scatter originates from use of new template for each data point. (b) L_d increases with drawing velocity; the MG demolds from the template at higher velocity (approximately 100 mm min^{-1}). (c) Similar increasing trend is observed for L_d shown as a function of cavity diameter.

The SEM images shown in figure 5 indicate that L_d is larger than L_e during the early stages of drawing. Also, $D_{\min}$ can be described by lubrication analysis without capillary term for short elongations. By substituting $D_{\min}$ from equation (2) and dropping out the L_e and constant terms, equation (10) can be reduced into a simple proportionality expression:

$$L_d \propto \eta v D_o, \tag{11}$$

According to this simplified model, L_d is directly proportional to the viscosity, the drawing velocity, and the cavity diameter. These predictions qualitatively agree with the experimental results (figure 6). Furthermore, equation (11) also predicts demolding when L_d exceeds the length of template cavity. Demolding was experimentally observed at higher drawing velocity and viscosity (figure 2), which is consistent with equation (11). Based on these observations, we believe that equation (11) captures the correct dependence of L_d on drawing parameters. The relation can be used to optimize the drawing conditions for rapid diameter reduction (small L_d) for efficient and practical nanomanufacturing.

3.4. Versatile nanomanufacturing

The understanding of thermoplastic drawing gained through experimental and theoretical analysis can be used to develop a robust manufacturing for MGs. Here we demonstrate two variants of the drawing technique for fabrication of geometries, which otherwise would be challenging to produce. In the first variant, a step change in velocity (up and down) was incorporated during drawing. In the second variant, rotational and vertical motion were superimposed during drawing. Figure 7 shows examples of Pt-MG fibers drawn using these protocols. A jump in drawing velocity from 1 to 60 mm min^{-1} generates very high aspect-ratio (>1000) nanowire from 200 μm structure (figure 7(a)). According to equation (11), initial slow velocity restricts the active liquid volume and results in rapid thinning under increasing capillary stress. Before the fiber diameter approaches necking instability, the elongation process transitions from capillary dominated (necking) to viscosity controlled (drawing) regime due to sudden increase in velocity. Consequently, a long nanowire is produced by neck-and-draw mechanism invoked through variation in strain-rate. Similarly, a step decrease in drawing velocity from 60 to 1 mm min^{-1} results in formation of microwire with nanotip through draw-and-neck mechanism (figure 7(b)). A combination of rotation and drawing yields twisted or threaded microfiber (figure 7(c)). Nanoscale fibers with similar corrugations are also feasible under optimal drawing and spinning conditions. Other drawing variants can be applied to fabricate complex MG geometries. Therefore, thermoplastic drawing of MGs is a simple and versatile technique for manufacturing of metal structures without lithography.

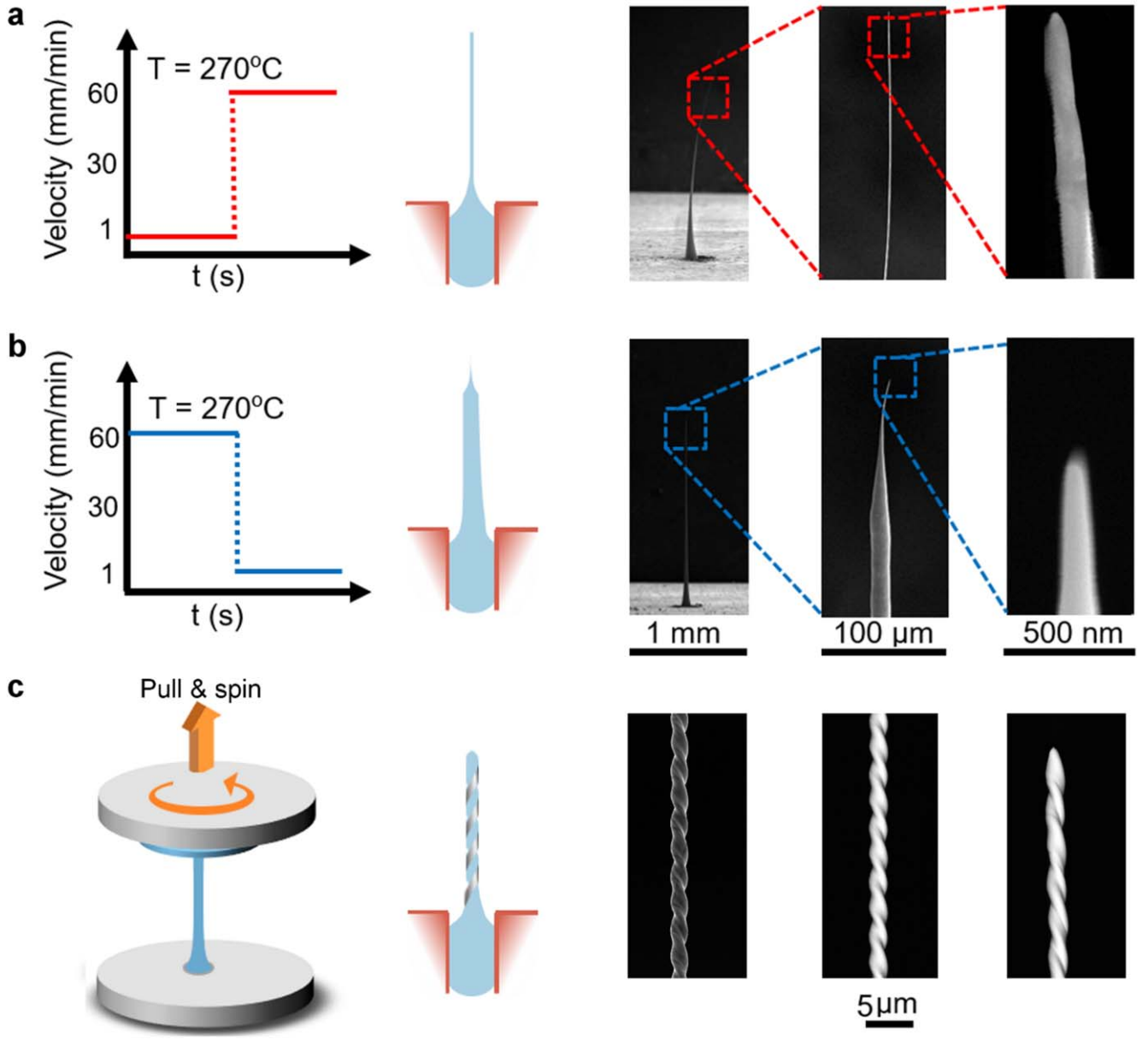

Figure 7. Variants of thermoplastic drawing technique. (a) Drawing velocity was increased from 1 to 60 mm min^{-1} after 30 s. A long nanowire (diameter $\sim$ 150 nm, length $>$ 200 μm) was produced through neck-and-draw mechanism. (b) Drawing velocity was decreased from 60 to 1 mm min^{-1}, resulting in formation of a microfiber with nanotip ($\sim$75 nm) produced through the draw-and-neck mechanism. (c) A threaded microfiber was formed by spinning the top plate at 200 rpm while drawing at velocity of 6 mm min^{-1}. All SEM images are from Pt-MG drawn at 270 °C using 200 μm diameter cavities.

4. Conclusions

This study provides a comprehensive description of size and shape evolution of MG supercooled liquid subjected to uniaxial tension. The elongation experiments are performed using Pt-Cu-Ni-P supercooled liquid filled in cylindrical cavities. We show that the shape of liquid filament produced during stretching is determined by the relative effects of capillary and viscous stresses (or equivalently by dimensionless capillary number). Large capillary number achieved through high-viscosity and/or elongation rate results in uniform thinning, whereas the liquid necks and ruptures with decreasing capillary number. The results can be explained without assuming non-Newtonian effects, in contrast to the mechanism suggested previously [42].

A phenomenological model based on combination of viscous lubrication analysis and capillary breakup of Newtonian threads accurately describes the evolution in diameter of MG fiber. The reduction in fiber diameter due to elongation is harnessed for lithography-free nanoshaping. We show that large MG structures can be downsized into nanoscale structures by manipulating the volume fraction of material subjected to elongation and the capillary stress. Experimental results reveal that the volume fraction of supercooled liquid involved in elongation can be controlled by varying the liquid viscosity, the elongation rate, and the cavity diameter. These

findings are rationalized based on crossover between the forces required for deformation and dewetting of metallic liquid from the cavity. The quantitative models proposed for evolution in diameter and active liquid volume can be used to control the outcome of MG drawing. Other drawing approaches such as, variable velocity and pull-and-spin are presented as proofs-of-concept to demonstrate the potential and versatility of drawing-based manufacturing.

Acknowledgments

This work was funded by the National Science Foundation (NSF) through CMMI Award#1663568 and NSF-CAREER Award#1653938. Microscopic characterization was performed using a Hitachi S-4300 SEM acquired through the NSF Major Research Instrumentation Program Award#0421032. We would like to thank Dr Molla Hasan for valuable discussions.

Author contributions

GK conceived the idea. ZH and CM conducted the experiments. JB developed the theoretical model. All authors analyzed the data and wrote the manuscript.

Notes

The authors declare no competing financial interest.

ORCID iDs

Golden Kumar https://orcid.org/0000-0001-5274-5715

References

[1] Ashby M F and Greer A L 2006 Metallic glasses as structural materials *Scr. Mater.* **54** 321–6
[2] Demetriou M D, Launey M E, Garrett G, Schramm J P, Hofmann D C, Johnson W L and Ritchie R O 2011 A damage-tolerant glass *Nat. Mater.* **10** 123
[3] Inoue A 2000 Stabilization of metallic supercooled liquid and bulk amorphous alloys *Acta Mater.* **48** 279–306
[4] Schuh C A, Hufnagel T C and Ramamurty U 2007 Mechanical behavior of amorphous alloys *Acta Mater.* **55** 4067–109
[5] Johnson W L 2013 Bulk glass-forming metallic alloys: science and technology *MRS Bull.* **24** 42–56
[6] Johnson W L 2002 Bulk amorphous metal—an emerging engineering material *JOM* **54** 40–3
[7] Wang W H, Dong C and Shek C H 2004 Bulk metallic glasses *Mater. Sci. Eng.* R **44** 45–89
[8] Greer A L 1995 Metallic glasses *Science* **267** 1947–53
[9] Sharma P, Kaushik N, Kimura H, Saotome Y and Inoue A 2007 Nano-fabrication with metallic glass—an exotic material for nano-electromechanical systems *Nanotechnology* **18** 035302
[10] Chen W-T, Manivannan K, Yu C-C, Chu J P and Chen J-K 2018 Fabrication of an artificial nanosucker device with a large area nanotube array of metallic glass *Nanoscale* **10** 1366–75
[11] Carmo M, Sekol R C, Ding S, Kumar G, Schroers J and Taylor A D 2011 Bulk metallic glass nanowire architecture for electrochemical applications *ACS Nano* **5** 2979–83
[12] Sekol R C, Kumar G, Carmo M, Gittleson F, Hardesty-Dyck N, Mukherjee S, Schroers J and Taylor A D 2013 Bulk metallic glass micro fuel cell *Small* **9** 2081–5
[13] Fukushige T, Hata S and Shimokohbe A 2005 A MEMS conical spring actuator array *J. Microelectromech. Syst.* **14** 243–53
[14] Henann D L, Srivastava V, Taylor H K, Hale M R, Hardt D E and Anand L 2009 Metallic glasses: viable tool materials for the production of surface microstructures in amorphous polymers by micro-hot-embossing *J. Micromech. Microeng.* **19** 115030
[15] Kumar G, Tang H X and Schroers J 2009 Nanomoulding with amorphous metals *Nature* **457** 868
[16] Kumar G, Desai A and Schroers J 2011 Bulk metallic glass: the smaller the better *Adv. Mater.* **23** 461–76
[17] Schroers J 2010 Processing of bulk metallic glass *Adv. Mater.* **22** 1566–97
[18] Saotome Y, Itoh K, Zhang T and Inoue A 2001 Superplastic nanoforming of Pd-based amorphous alloy *Scr. Mater.* **44** 1541–5
[19] Hu Z, Gorumlu S, Aksak B and Kumar G 2015 Patterning of metallic glasses using polymer templates *Scr. Mater.* **108** 15–8
[20] Hasan M, Schroers J and Kumar G 2015 Functionalization of metallic glasses through hierarchical paetterning *Nano Lett.* **15** 963–8
[21] Li N, Chen Y, Jiang M Q, Li D J, He J J, Wu Y and Liu L 2013 A thermoplastic forming map of a Zr-based bulk metallic glass *Acta Mater.* **61** 1921–31
[22] Ma J, Huo L S, Zhao D Q and Wang W H 2013 Micro mold filling kinetics of metallic glasses in supercooled liquid state *J. Appl. Phys.* **113** 104505
[23] Liu L, Hasan M and Kumar G 2014 Metallic glass nanostructures: fabrication, properties, and applications *Nanoscle* **6** 2027–36
[24] Kumar G, Blawzdziewicz J and Schroers J 2013 Controllable nanoimprinting of metallic glasses: effect of pressure and interfacial properties *Nanotechnology* **24** 105301
[25] Zhao M, Abe K, Yamaura S-I, Yamamoto Y and Asao N 2014 Fabrication of Pd–Ni–P metallic glass nanoparticles and their application as highly durable catalysts in methanol electro-oxidation *Chem. Mater.* **26** 1056–61
[26] Sekol R C, Carmo M, Kumar G, Gittleson F, Doubek G, Sun K, Schroers J and Taylor A D 2013 Pd–Ni–Cu–P metallic glass nanowires for methanol and ethanol oxidation in alkaline media *Int. J. Hydrog. Energy* **38** 11248–55
[27] Padmanabhan J, Kinser E R, Stalter M A, Duncan-Lewis C, Balestrini J L, Sawyer A J, Schroers J and Kyriakides T R 2014 Engineering cellular response using nanopatterned bulk metallic glass *ACS Nano* **8** 4366–75
[28] Päivänranta B, Merbold H, Giannini R, Büchi L, Gorelick S, David C, Löffler J F, Feurer T and Ekinci Y 2011 High aspect ratio plasmonic nanostructures for sensing applications *ACS Nano* **5** 6374–82
[29] Huang J-A, Zhao Y-Q, Zhang X-J, He L-F, Wong T-L, Chui Y-S, Zhang W-J and Lee S-T 2013 Ordered Ag/Si nanowires array: wide-range surface-enhanced Raman spectroscopy for reproducible biomolecule detection *Nano Lett.* **13** 5039–45
[30] Ma X *et al* 2016 Sharp-tip silver nanowires mounted on cantilevers for high-aspect-ratio high-resolution imaging *Nano Lett.* **16** 6896–902
[31] Ye S, Rathmell A R, Stewart I E, Ha Y-C, Wilson A R, Chen Z and Wiley B J 2014 A rapid synthesis of high aspect

ratio copper nanowires for high-performance transparent conducting films *Chem. Commun.* **50** 2562–4
[32] Lee J-Y, Connor S T, Cui Y and Peumans P 2008 Solution-processed metal nanowire mesh transparent electrodes *Nano Lett.* **8** 689–92
[33] Tarigan H J, Kahler N, Ramos N S, Kumar G and Bernussi A A 2015 Low reflectance of nano-patterned Pt-Cu-Ni-P bulk metallic glass *Appl. Phys. Lett.* **107** 021903
[34] Uzun C, Kahler N, Grave de Peralta L, Kumar G and Bernussi A 2017 Photo-induced heat localization on nanostructured metallic glasses *J. Appl. Phys.* **122** 094306
[35] Nakayama K S, Yokoyama Y, Ono T, Chen M W, Akiyama K, Sakurai T and Inoue A 2010 Controlled formation and mechanical characterization of metallic glassy nanowires *Adv. Mater.* **22** 872–5
[36] Wu B, Heidelberg A and Boland J J 2005 Mechanical properties of ultrahigh-strength gold nanowires *Nat. Mater.* **4** 525
[37] Peng C, Zhan Y and Lou J 2012 Size-dependent fracture mode transition in copper nanowires *Small* **8** 1889–94
[38] Kulkarni A J and Zhou M 2006 Size-dependent thermal conductivity of zinc oxide nanobelts *Appl. Phys. Lett.* **88** 141921
[39] Yi J, Bai H Y, Zhao D Q, Pan M X and Wang W H 2011 Piezoresistance effect of metallic glassy fibers *Appl. Phys. Lett.* **98** 241917
[40] Huang Q, Lilley C M, Bode M and Divan R 2008 Surface and size effects on the electrical properties of Cu nanowires *J. Appl. Phys.* **104** 023709
[41] Yi J, Xia X X, Zhao D Q, Pan M X, Yang B H and Wang W H 2010 Micro-and nanoscale metallic glassy fibers *Adv. Eng. Mater.* **12** 1117–22
[42] Hasan M and Kumar G 2017 High-throughput drawing and testing of metallic glass nanostructures *Nanoscale* **9** 3261–8
[43] Hasan M and Kumar G 2016 High strain rate thermoplastic demolding of metallic glasses *Scr. Mater.* **123** 140–3
[44] Yao M, McKinley G H and Debbaut B 1998 Extensional deformation, stress relaxation and necking failure of viscoelastic filaments *J. Nonnewton. Fluid. Mech.* **79** 469–501
[45] Gaudet S, McKinley G H and Stone H A 1996 Extensional deformation of Newtonian liquid bridges *Phys. Fluids* **8** 2568–79
[46] Dodds S, Carvalho M D S and Kumar S 2009 Stretching and slipping of liquid bridges near plates and cavities *Phys. Fluids* **21** 092103
[47] Legg B A, Schroers J and Busch R 2007 Thermodynamics, kinetics, and crystallization of $Pt_{57.3}Cu_{14.6}Ni_{5.3}P_{22.8}$ bulk metallic glass *Acta Mater.* **55** 1109–16
[48] Pitt E B, Kumar G and Schroers J 2011 Temperature dependence of the thermoplastic formability in bulk metallic glasses *J. Appl. Phys.* **110** 043518
[49] Harmon J S, Demetriou M D and Johnson W L 2007 Rheology and ultrasonic properties of $Pt_{57.5}Ni_{5.3}Cu_{14.7}P_{22.5}$ liquid *Appl. Phys. Lett.* **90** 171923
[50] Kumar G, Rector D, Conner R D and Schroers J 2009 Embrittlement of Zr-based bulk metallic glasses *Acta Mater.* **57** 3572–83
[51] Renardy M 1994 Some comments on the surface-tension driven break-up (or the lack of it) of viscoelastic jets *J. Nonnewton. Fluid. Mech.* **51** 97–107
[52] Papageorgiou D T 1995 On the breakup of viscous liquid threads *Phys. Fluids* **7** 1529–44
[53] McKinley G H and Tripathi A 2000 How to extract the Newtonian viscosity from capillary breakup measurements in a filament rheometer *J. Rheol.* **44** 653–70
[54] Tadmor R, Das R, Gulec S, Liu J, N'guessan H E, Shah M, Wasnik P S and Yadav S B 2017 Solid–liquid work of adhesion *Langmuir* **33** 3594–600
[55] Boreyko J B and Chen C-H 2009 Restoring superhydrophobicity of lotus leaves with vibration-induced dewetting *Phys. Rev. Lett.* **103** 174502